

B¹⁰-pellet Fluidized-Bed for D-He³ Fusion Reactor Shielding

Giovanna Nucci^a, Sophia Capili^b

^aPrinceton University, Mechanical and Aerospace Engineering,

^bPrinceton University, Chemical and Biological Engineering,

Abstract

The use of fluidized boron particles as a method of neutron shielding and heat exchange for D- 3 He burning fusion reactors, such as the Princeton Field Reverse Configuration (PFRC) type, was explored via experiment and modeling. A column of 0.6-cm-diameter Delrin precision balls was fluidized by air in single 4.1-cm-ID 50-cm-long cylinder. In the column, fluidization was achieved at gas flow rates near 0.3 m/s and pressure gradients of 10 Pa/cm and burst-height instabilities observed. At the column's walls, the outer layer of balls was often stationary, an effect attributed to steric hindrances. Computational fluid dynamics using ANSYS software and discrete element method (DEM) simulations using Altair software were performed to test their applicability to annular configurations.

Keywords: fluidized bed, heat exchanger, neutron shielding, X-ray heating

1. Introduction

The Princeton Field Reverse Configuration (PFRC) reactor is a fusion reactor that burns deuterium and helium-3 – an aneutronic reaction. However, the small number of secondary D-D and D-T reactions results in a small amount of neutron production. Neutron bombardment poses structural damages and is considered as the most dangerous form of radiation to humans, and thus shielding is needed to protect the reactor and its operators. Additionally, the PFRC emits power in the form of X-ray power primarily from the bremsstrahlung and synchrotron

1.1. Problem statement

The simplest approach to the shielding problem is solid shielding and heat capture material surrounding the fusion-reactor. Neutron shielding requirements are not yet easily calculated, but for now one can assume that the the X-ray shielding requirements for heat capture are sufficient. Approximating from an attenuation length graph of X-rays at 30 keV ¹, the attenuation length of an X-ray at the order of 200 keV can be assumed to be the same at about 3 cm given the constant profile in higher keV. Since $1/e$ of the X-ray power is deposited in every 3 cm, setting the thickness at ten-fold the attenuation length provides 99.5% of X-ray shielding. Given the dimensions of the a cylindrical shell in Figure 2 where the inner diameter surrounds the plasma, about 30 cm of shielding thickness required [5]. Following through with solid shielding, however, poses several problems, namely stresses due to thermal expansion and reaching critical temperature for boron electrical conductivity – which interferes with RF plasma heating. Additionally, energy from neutron bombardment as well as radiation should be extracted at high efficiency for conversion to electricity. Solely relying on heat conduction through a thick solid shell would not suffice, so some sort of channels are needed to have an efficient heat exchanger.

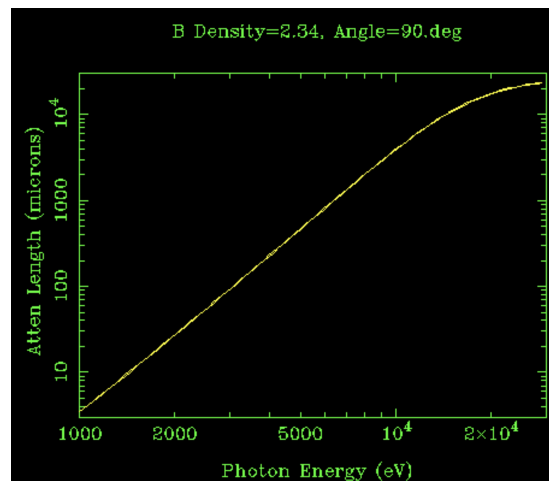


Figure 1: X-ray attenuation graph for pure boron.

1.2. Rationale

A fluidized bed of boron-tungsten pellets levitated by gas addresses these issues: space between the boron pellets minimizes stresses by reducing mechanical contact through levitation, and the constant cooling allows temperature control over the boron pellets, decreasing electric conductivity. Levitation occurs as the pressure drop over the particle overcomes the force of gravity on the particle. On a whole bed level this can occur over the entire bed causing fluidization of the entire bed. Mixing within the bed also allows a more ideal power dispersion, whereas the solid boron solution would have a power distribution concentrated around the inner cylinder. Creating channels would no longer be of concern, and the nature of the fluidized bed allows more gas-solid contact for increased heat transfer.

Common fluidized bed designs follow that of Cocco et al. which comprises of a plenum, gas distributor, heating/cooling

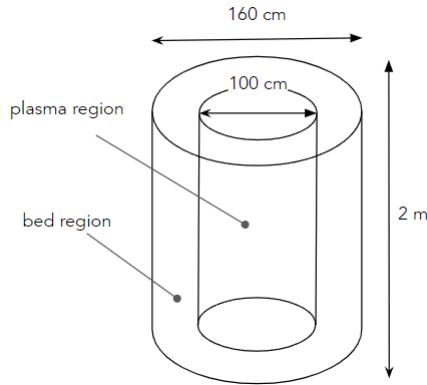


Figure 2: Intended full-scale dimensions for the fluidized bed.

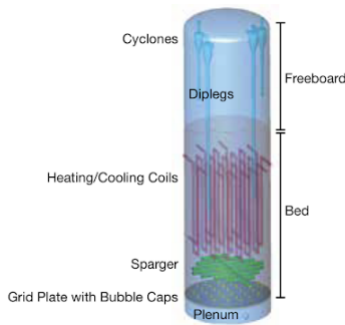


Figure 3: Typical fluidized bed setups, adapted from Cocco et al., 2014. [3]

coils, the bed itself, and cyclones (i.e. pellet recuperators) [3]. For the purposes of this project, the final design most likely will adapt only the plenum, gas distributor, and the bed itself. This design does not implement coils and cyclones because (1) the pellets themselves are the source of heat from absorbing X-rays and (2) a mesh will be used to prevent pellets escaping. In addition to the typical vertical cylinder geometry, horizontal configurations will be considered as well, introducing an avenue of other design decisions needed to prevent instabilities.

Diverging from common designs requires both simulations and experiments in order to properly understand what working parameters are best for the given problem statement as well as what instabilities to be wary of. The definition of "instabilities" used here are essentially features that arise during the operation of the fluidized bed that result in non-homogeneity, such as bubbles or regions of drastically different movement patterns.

2. Methods

Fluidized beds have complex hydrodynamics, and the addition of problems such as neutron shielding, X-ray shielding, and heating make it more difficult to optimize working conditions. Hand calculations, simulations, or experiments alone are not sufficient to quantify different parameters, so simultaneously using all three for each set-up helps fill in missing parameters and validate calculations and data.

The experiments conducted are important for giving physical form and validity to the concepts that appeared throughout lit-

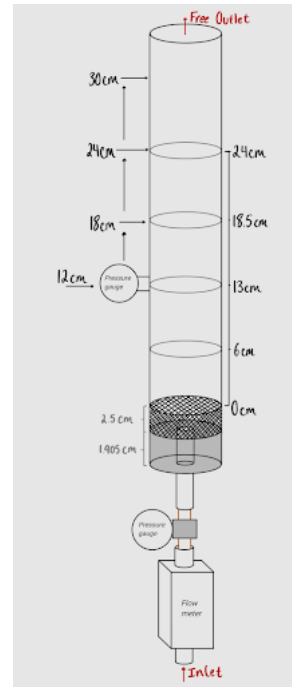


Figure 4: Diagram of the single-cylinder experiment.

erature. Additionally they are necessary for revealing areas of greater instability than expected from simulated and modeled results.

Computational fluid dynamics (CFD) is useful for studying the behavior of gas within a porous bed. For the purposes of this project, it is a faster way to study gas behavior at different setups. The CFD software used here were Ansys Fluent and Altair's Hyperworks CFD. Discrete element method (DEM) is another popular tool to more accurately represent and study fluidized beds, and the software used here is Altair's EDEM which can be coupled with Hyperworks CFD. Instead of a porous bed, DEM simulates particle behavior by calculating force equations on each particle. The two are often coupled as CFD-DEM: Boundary conditions (i.e. gas flow, heating, electrostatics) are set up in CFD software, and the outputs of the CFD simulation are ported into DEM input. The result is an animation of the fluidized bed, enabling studies of its bubbling behaviors and other parameters such as velocity, pressure, temperature, and heating.

2.1. Design criteria

The experiments and simulations that follow all aim to provide benchmarks for the following design decisions:

- Ball diameter ranges
- Neutron shielding thickness
- X-ray shielding thickness
- Inlet velocity ranges (limited by fluidization and heating)

An acceptable fluidized bed should be homogeneous, maintain temperatures below boron's critical temperature of about 1100K for conductivity, and safe from mechanical and thermal stresses.



Figure 5: The experimental single-cylinder configuration above has a 24 cm starting bed height with the bottom mesh setup. Two pressure gauges are shown, each an SSI Technologies, LLC digital gauge with an accuracy of ± 0.001 psi, the first is located just below the inlet and the second is located 6 cm above the starting bed height at a height of 30 cm.

2.2. Single-cylinder Experiment set-up

To simplify the problem and gain intuition, experiments and simulations were set up using a single cylinder geometry instead of the intended annular geometry.

2.2.1. Experimental Process

The experiment set-up in Figure 3 features a vertical tube and inlet of gas at the bottom opening. Experiments were run at 6cm with different mesh configurations as shown in Figure 6. The primary experimental set-up included a mesh that raises the bed to create a plenum for gas distribution, an inlet velocity flow meter, precision pressure meters placed at the inlet, and another pressure meter that is vertically adjustable to set at different bed heights. Although the no mesh and the top and bottom mesh configurations were experimented with, the primary setup of focus included only the bottom mesh. The bottom mesh was meant to enable better gas distribution to the entirety of the bottom particles instead of the more localized opening shown in the no mesh setup in Figure 6. Inlet velocities reported for the bottom mesh configurations are all diffused inlet velocities which were calculated using mass conservation between the localized inlet area to the area of the mesh. The small inlet area was $1/4''$ and the mesh area was $15/8''$.

Bursting and collapsing pressure calculations were conducted using equations C.1 [8] and C.2 [12] with a safety factor of 2. The material constants used for these calculations can be found in Table C.7, additionally, all nomenclature and symbolology can be found in Table C.5. The 73 (Phantom v7.3) Fast Camera was the primary method of recording the bed's behavior. All camera data was collected at 250 frames per second with an exposure time of $3900 \mu s$ in black and white.

Each trial was conducted using air as the fluid and Delrin precision balls as the particles. The experiments conducted are specified in Table 1 and the experimental setup specifications can be found in Table 2. For each configuration and bed height each trial consisted of first readying the fast camera and then

Table 1: Experiments Conducted

Mesh Configuration	Settled Bed Height (cm)
No mesh	6
Top and bottom mesh	6
Bottom mesh	6
	13
	18.5
	24

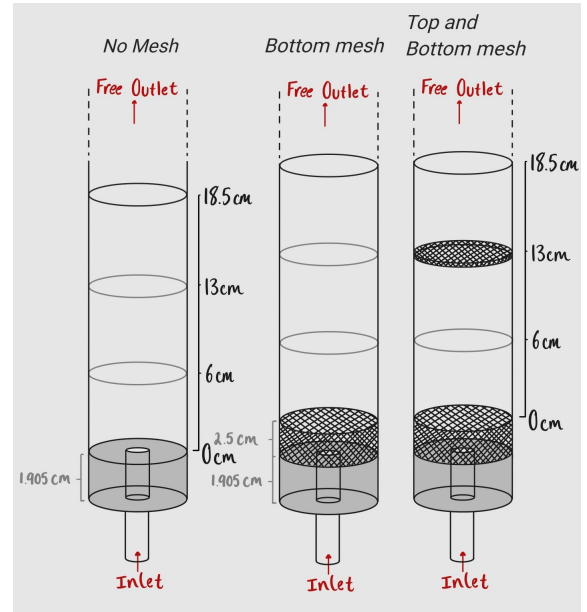


Figure 6: Experimental configurations given mesh, bottom mesh, and bottom and top mesh set-ups.

turning the inlet flow at the gas tank. After the fast camera data was collected—between 5 to 10 seconds—the pressure at the inlet and at approximately 6 cm above the resting bed height was recorded with the volumetric inlet flow rate and the max bed height. Observations were additionally noted throughout experimentation. The pressure at the gas tank was varied by 2.5 psi starting from 20 psi until around 42.5 psi. After this point the pressure was increased in varying intervals of 2.5, 5, or 10 psi for observational areas of interest.

2.2.2. Ansys - Simulation

A series of simulations were set up in increasing complexity to understand fluidization behaviors in Figure 7. The simplest simulation consisted of a static model of an incipient fluidized bed conducted using Ansys software. Assuming face-centered cubic arrangements of pellets, the void space was modeled through CAD with varying pellet diameters and bed heights. All CAD geometries were created using 10% Gaussian of the given particle diameter spacing between particles for either FCC or BCC configurations. Although a body centered cubic configuration was made it was not simulated due to time constraints. A no-slip boundary condition along the walls as well as various inlet gas velocities were applied through CFD. A vertical 1D pressure profile placed along the center-line of

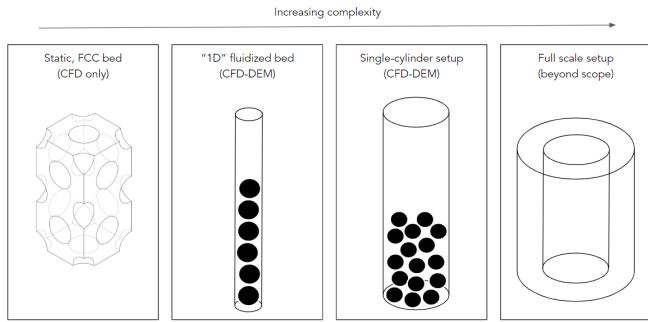


Figure 7: Series of simulations in increasing complexity, each providing different observations and data.

the geometry was monitored to compare to Ergun equation C.3 calculations for the expected pressure drops across a single particle and across different bed heights. Along with bed height and pellet diameters the model parameters were also varied by changing the flow model to either laminar, low-turbulent, or high turbulent modes. The simulations conducted can be found in Table A.4. The simulations were limited by time and license capabilities and therefore only select CAD configurations could be run and only certain parameters could be tested for influence on the overall flow.

2.2.3. Ansys - CAD

The geometries that were made include the following particle diameters: 6 mm, 2 mm, 1 mm, and 0.5 mm. The 6 mm particle diameter was simulated the most as it corresponds with the experimented particle size and proved to be the easiest to simulate given software limitations which will be described [say were]. 6 mm particle geometries created include 2 row configurations for FCC and body centered cubic (BCC). This was the only instance in which a BCC set-up was created; all following models will be based on a FCC unit cell. The equations used to calculate the measurements and geometry for the FCC geometry are as follows: equation C.12 was used to calculate the smallest distance scale, equation C.13 was used to calculate a standard FCC unit cell's height, and finally equation C.14 calculated the overall bed height of the simulation. For each given particle diameters geometries in FCC configurations were made with 2 row, 10 row, 20 row, 30 row, 40 row, and 100 row lengths. Each row corresponds to a single unit cell height based on the given particle size for which the math and methodology can be found in figure [create figure for math and geometry calculations]. The non-diameter specified CAD models used can be found in Figure 8.

2.2.4. Ansys Limitations

In order to simulate the flow through different geometries with varying parameters a mesh was first created for the specified geometry. As the particle size gets smaller, so does the mesh cell size which causes the simulation itself to run slower based on computing power. Additionally a student license was used during certain simulations which limits the total number of cells allowed. This means a larger mesh was run for cer-

Simulation Geometries - Face Centered Cubic

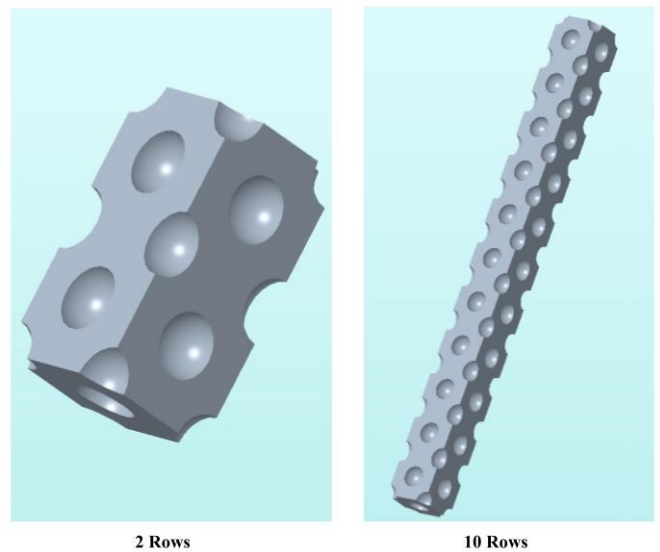


Figure 8: Used simulation CAD geometries with non-specified particle diameter in face centered cubic configuration. The particles geometries used are as follows: 6 mm, 2 mm, and 1 mm.

tain simulations. A larger mesh size leads to faster computations but may not capture fluid regions with enough accuracy to understand the flow overall. For these reasons only certain geometries were run which are detailed in Table A.4.

2.2.5. DEM - Simulations

The next set-up introduced DEM into the workflow. A "1D" column was set wherein the diameter enabled only a single column of balls with a small amount of space on the side to enable gas-particle interactions across the entire bed. Materials were imported into the simulation to represent proper particle-particle and particle-wall interactions, and the same geometry dimensions were maintained. After the geometry was made through CAD, boundary conditions were added in Hyperworks CFD: an inlet flow rate of air and no-slip conditions at the wall. In EDEM, a cylindrical particle factory is formed to produce one ball each. For all DEM simulations here, particles were set to simultaneously generate in the beginning of the simulation, as near to $t = 0$ as possible, and factory was set to be "static" meaning the particles are held in place until all particles are formed in order to properly reflect startup behaviors.

The next simulation is a more ideal representation of the system and comprised of a single cylinder geometry to represent the fluid domain and the balls. Again, materials were imported into the simulation to represent proper particle-particle and particle-wall interactions, and the same geometry dimensions were maintained. The primary purpose of this simulation is to observe discrepancies between the experiment and the ideal conditions in the simulation, which can be usually explained by external forces not accounted for in CFD-DEM. After the geometry was made through CAD, boundary conditions were added in Hyperworks CFD: an inlet flow rate of air and no-slip conditions at the wall. In EDEM, a particle factory

Table 2: Experiment set-up specifications.

Property	Value
Cylinder diameter	1 $\frac{5}{8}$ in
Cylinder material	Polycarbonate
Ball diameter	6 mm
Ball material	Delrin
Working fluid	Air
Particle Packing Efficiency	58%

was made within the geometry in the form of a cylinder that is virtual (as in, it is not a physical object) with the same diameter as the pipe and with a desired bed height as its length. The number of particles were arbitrarily set by iterating over different amounts until the desired bed height was achieved.

2.3. Small-scale annular setups

The final geometry of the fluidized bed is a hollow annulus, which can be oriented vertically or horizontally depending on the instance (e.g. horizontally in vehicles for disaster cites). An annulus is an uncommon geometry used for fluidized beds, and horizontal orientations are even more so. Thus, the small-scale annular setup provides qualitative information about what instabilities occur in these uncommon configurations. Due to the complexity of the geometry more simulations need to be conducted; however, when possible Ansys simulations were done assuming a periodic boundary condition for parallel walls. This implies the visualized flow will be the same all around and the single row flow is then reflective of the annular flow assuming there is appropriate diffusing of the inlet flow. Unfortunately due to time constraints and poorly distributed inlet flow appropriate experimentation could not be done on this configuration.

3. Results

3.1. Ansys Simulation Results

3.1.1. Pressure and Velocity Profiles

Figures A.21 through A.24 show velocity and pressure profiles from Ansys simulations. The primary parameters that were varied include: particle diameter, inlet velocity, and flow model (laminar, low-turbulence, high-turbulence). As expected there are higher pressure regions towards the inlet and lower pressure regions towards the outlet. Particles have higher pressure regions directly below particles where the flow stagnates and then proceeds around the particle. Locations with the greatest space between particles have the most consistent gradient of pressure [fix this setting]. As the flow velocity increases more flow regions can be seen. Figure 9 shows the velocity profile given a laminar flow model for varying inlet velocities and the 6mm particle geometry. The gradient of the flow becomes more extreme [does this make sense] with inlet velocity however the overall shape of the flow does not. The greatest variance can be seen in the regions directly after particles. The flow after the particle has a region of low velocity which for our purposes is

the wake of the flow. For the inlet velocity 0.1 m/s the wake is much smaller and more consistent in its overall upward pointed direction as compared to the other velocities. As the flow increases there is more variety in the overall direction of the wake, pointing left or right. This is seen at an inlet velocity of 1.5 m/s where the wake has lengthened, is less uniform, and has varying tilts. The first wake for each velocity has a seemingly uniform velocity throughout even if the wake size has increased with velocity.

Figure A.22 shows the pressure profiles for different diameters given a consistent inlet velocity of 1 m/s . The pressure profile for 1 mm and 2 mm diameter particles shows little difference in overall appearance; however, the pressure variation for 1 mm was significantly less than the 2 mm geometry. Additionally, the 2 mm pressure scale shows a max pressure of 9.996 Pa but the majority of the pressure profile, even at the inlet, does not indicate any pressure in the orange or red range. Due to the difference in scaling it is difficult to discern which components are valid and useful from these pressure profiles and should be considered during analysis. The 6 mm geometry shows more distinct flow regions which could be due to greater instabilities in the flow due to a larger geometry or could be due to outside influences such as the ability of the simulation mesh to represent the flow in a detailed manner. All simulation mesh settings can be found in Table 1. For the 6 mm geometry the height for which the pressure has gone to approximately zero is closer to the outlet compared to the 2 mm and 1 mm geometries. This same occurrence can be seen between 1 mm and 2 mm geometries although the difference is less discernible in comparison with the 6mm geometry. Figure A.23 shows the pressure profiles for 6mm particles with 2 rowed FCC configurations. In this figure, the inlet velocity, 0.5 m/s , and particle diameter were consistent while the flow model was varied. The low turbulence model shows the most distinct flow regions; however, each flow model does show approximately the same pressure profile. In this instance, there is little difference between the laminar and high turbulence models. The relatively minor variance between the different flow models is likely due to the low inlet velocity that doesn't result in enough instabilities in the flow for the different models to then indicate a further variance in the flow. Figure A.24 displays different flow models for a high inlet velocity of 350 m/s using the 2mm geometry. Given the higher velocity, it was predicted the higher turbulence model would fit best. The high turbulence model has the lowest max pressure where the laminar model has the highest max pressure. This indicates more of the flow is understood by the high turbulence model and therefore results in a lower max pressure. The simulation meshing used for Figure A.24 was not fine which ultimately meant visual discrepancies in the 2D pressure and velocity profiles could not be discerned. A more fine mesh should be used upon further simulations.

3.1.2. Pressure and Velocity Graphs

The simulation pressure and velocity data were compiled into graphs A.15 through A.20. For Figures A.15 and A.17 to A.20 the pressure drop profile over the bed and over a singular particle shows a linear pressure drop as well as consist pressure

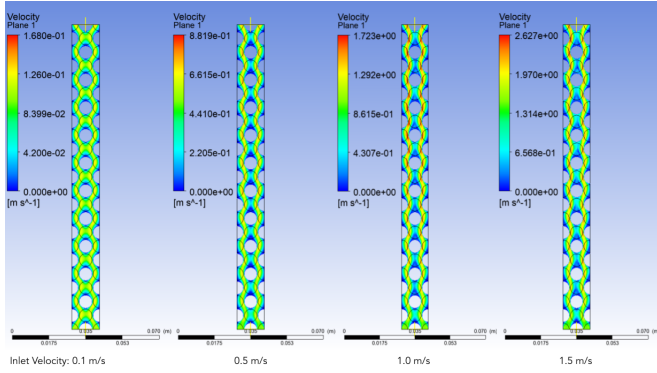


Figure 9: 2D velocity profiles given varying inlet velocities for 6 mm particle diameter configurations showing flow patterns. Increasing instability is seen with increasing velocities.

fluctuations between particles which. The pressure profile between particles will be referred to as the in-between pressure. The primary variation in this shape occurs when varying the flow model at high velocity or varying the inlet velocity for a specific flow model. As depicted in Figure A.15, which varied inlet velocity for the 2 mm 10 row geometry in FCC configuration, the pressure drop between a particle remained consistent across the bed. The pressure profile between particles, excluding the initial pressure data which occurred after the first particle, is composed of a starting bump into a dip that rises to the highest point. The tail ends of the in between pressure sections represents the stagnant pressure where the flow reaches the next particle. The inlet velocities ranged from 0.1 to 1.6 m/s in varying intervals. The total bed pressure drop linearly decreased with an increasing negative slope as the velocity increased. This can be seen further comparing the larger inlet pressure variance with the lower outlet pressure variance.

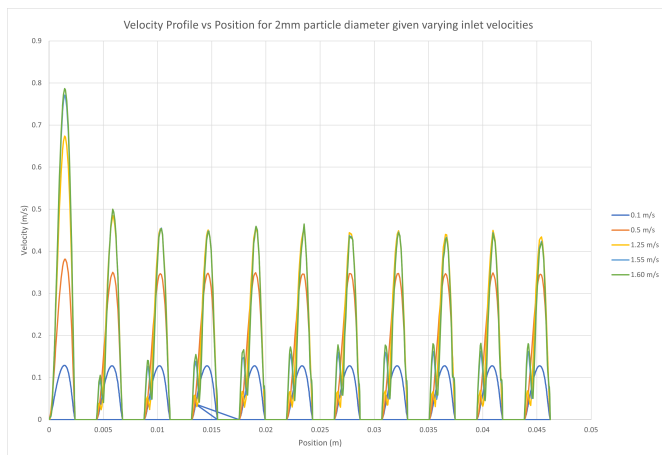


Figure 10: 1D Velocity Profile through 10 row FCC configuration for 2 mm diameter particles.

Although the in-between pressure profile was generally consistent across experimentation, variance can be seen in the tail end of each in-between pressure section. This occurred when changing the flow model at high inlet velocities in Figures A.17 and A.18. These figures show the 1D pressure profiles for 2mm

10 row geometries with varying flow models at inlet velocities of 250 and 350 m/s respectively. For both velocities the tails of in-between pressure sections show a larger increase in pressure for the Laminar and Low turbulence flow models. The overall pressure is also higher and has a less consistent total bed pressure drop as compared with the high turbulence flow model. This is especially clear for the 350 m/s inlet velocity. This may indicate, at 250 m/s , the flow is in between high and low turbulence models. In both cases the max inlet pressures are highest for the laminar flow and decrease from low to high turbulence models. Figure A.19 shows varying high inlet velocities for the laminar flow model using the 2 mm 10 row geometry. In this figure, the inlet velocities 250 and 300 m/s have similar pressure profiles, where as, at the inlet velocity of 350 m/s the tail end of the in-between pressures increase more rapidly. This could indicate the laminar flow model is not appropriate for an inlet velocity of 350 m/s . Figure A.20 similarly varies the flow model but given a 0.5 m/s inlet velocity and a 2 row 6 mm geometry. The difference between the pressure profile, in this instance, doesn't present the same rapid increase in the tail ends. The profiles overall are similar in shape to one another. The low turbulence profile is about 0.02 pa above the other flow models and the laminar and high turbulence models are often on top of one another.

Figure 10 shows the velocity profile for the 2 mm 10 geometry at varying initial low inlet velocities given the laminar flow model. The maximum velocity is at the first velocity peak. After the initial peak, each subsequent velocity peak, which occurs between each particle, lowers significantly and is relatively consistent over the rest of the bed. Figure A.16 shows pressure drop versus inlet velocity for the 2 mm 10 row particle geometry over a range of low inlet velocities given the laminar flow model. The data shows a linear relationship between pressure drop and inlet velocity.

The simulation pressure drop data for the 2 mm geometry at varying low inlet velocities was compared with pressure drop calculations completed using Ergun's Equation, C.3 [4], in Figure 14. The simulated pressure drop is lower and linear as compared with the much higher calculated Ergun pressure drop that is not linear.

3.2. Single Cylinder - Experimental Results

3.2.1. Fast Camera Data

Results from the fast camera imaging revealed how fluidization occurs and the instabilities that are present in this experimental set-up. Figures B.28 to B.33 contain fast camera images. The primary observations include: varying particle burst heights, bed separation upon start-up, particle trapping with a constricted top, multiple bed separations with large starting heights, stable cylindrical shell particle formation, bed height and spout settling, oscillating bed segments, inconsistency in bed separation locations. These observations, although shown separately in many figures, are often related to one another.

Figures B.28 and 12 show images that have both top and bottom mesh. This was done with a 6 cm starting bed height at an inlet velocity of 0.406 m/s and 0.414 m/s respectively. After

the initial flow start-up, in Figure B.28, the particles became trapped in a stable pattern at the top of the mesh. At 0.836 seconds trapped particles started to become loose; although, it was only when the bed continued to pulse, the duration of which lasted from 0.760 to 1.868 seconds, that the layer of trapped particles thinned and completely dropped. Figure 12 shows a larger number of particles were trapped and were stable for longer when start-up occurred at a higher inlet velocity.

Figure B.29 highlights the different sections of fluidized particles over time given a 24 cm starting bed height and an inlet velocity of 0.419 m/s. The primary bed sections displayed are as follows: stationary particles, levitating particles, rising particles, and falling particles. After flow start-up the bed rises in one large section with bed separation occurring close to the inlet. At 0.396 seconds the rising layer begins to break a part and particles from the bottom start to fall. At 0.868 seconds bed separation begins to occur again, however, as particles continue to fall from the top bed there is a section that levitates as it tries to rise but is prevented from doing so due to actively falling particles above it. Although particles continue to fall onto the levitating section and continue to separate from the bottom of the levitating section, eventually the force pushing on the levitating section overpowers the weight of the relevant particles and begins to rise again. After multiple bed separations occur the levitating particles can be seen at 1.796 seconds to occur in two locations in the overall fluidized bed.

The location of bed separation changed over time as seen in Figure B.32. At 0.180 seconds into fluidization bed separation occurs at approximately 1.2 cm. The subsequent separation increases to 4.2 cm at 0.672 seconds. After 3.452 seconds bed separation has begun to regularly occur at three times that height. Below where this occurs the bed is close to perfectly packed below the indicated red line. These particles are perfectly packed all around the cylinder which creates an outer column where the particles are stable. Particles inside and separate from the stable particle column remain fluidized. Figure B.32 depicts how close packing effects the height where bed separation occurs which is in part due to the outer column formation. The outer column likely forms due to electrostatic and friction forces between particles.

At lower inlet velocities the particle bed settles into a lower bed height than the max spurt height which often occurs at or near start-up. This is shown in Figure B.30 which has a 0.310 m/s inlet velocity and a 13cm starting bed height. At 0.948 seconds from start-up the bed bursts to its max height, approximately 0.12 cm above the initial height, at 1.42 seconds the bed settled to a lower height of around 0.10 cm above resting bed height. The settled bed height was consistent over a span of at least 2 seconds. After settling, the particles in the bed vibrated and upon flow shot off remained at the settled height.

Figure B.31 shows bed separation height oscillation given a 0.388 m/s inlet velocity and a 13 cm starting bed height. After flow start-up at 0.884 seconds, bed separation occurred at a 4.0 cm from the bottom and at 0.960 seconds this increased to 4.6 cm. Over the span of the next 0.260 seconds the bed separated 3 times until 1.220 seconds in. After each separation the location increased until, at 1.220 seconds, the location of separation

was approximately 8.1 cm. Then, at 1.372 seconds, the bed separated at 5.3 cm and increased to 7.1 cm at 1.572 seconds. This indicated an oscillation of the bed separation location. A changing bed separation height can also be seen in Figure 13; however, here the height of bed separation settled after 1.516 seconds and did not oscillate. The areas indicated in blue represent areas where the particles are packed such that they tend to hold a patterned configuration. Oscillating behavior were also seen in max bed height measurements as indicated in Figure B.33. Given a 24 cm starting bed height and an inlet velocity of 0.375 m/s, Figure B.33 shows the change in max height at each bed spurt from 0.536 to 5.032 seconds.

3.2.2. Experimental Graphs

Figure B.25 shows the pressure drop versus inlet velocity for the mesh and no mesh experimental set-ups shown in Figure 6. The no mesh set-up has distinct outliers in the data and there is no linear trend in the data as seen in the mesh (top and bottom) set-up. Both data sets indicate a positive relationship between pressure drop and inlet velocity. This positive relationship is further seen in Figure B.26. Here the bed height was varied while pressure drop and inlet velocity were recorded. Although pressure drop seems to increase with bed height, the data is extremely clustered and it is difficult to ascertain the shape and relationship overall. In Figure B.27 the inlet velocity and corresponding bed height were recorded to show bed height variation over different inlet velocities for a given starting bed height. As starting bed height increases the positive slope of each data set increases.

3.3. DEM Simulations

3.3.1. "1D" model

Given arbitrary default materials in the EDEM program with, a coarse visualization of a most basic fluidized bed is observed. Figure 11 shows the start-up fluidization behavior for an input velocity of air that is beyond incipient fluidization, as exhibited by the particles' positions above. The particles are 3 mm in radius with a 0.16 m/s gas inlet velocity. After all of the particles are generated and maintained at a static position after 1 second has passed, all three balls levitate at the same time. It is important to note, however, that the balls are not perfectly rested on top of one another because of the random nature of particle factories.

3.3.2. Simple-cylinder model

For the DEM simulations, 13 cm bed heights were arbitrarily chosen to minimize the amount of particles to generate. The points of interest in Table 3 are the conditions at which the bed starts to fluidize.

With an inlet of 0.432 m/s, the simulation shows little to no movement in the bed. An inlet of 2.5 m/s also shows no movement in the bed. Further debugging needs to be conducted as heavy slugging was observed in experimental data at these ranges of inlet velocities.

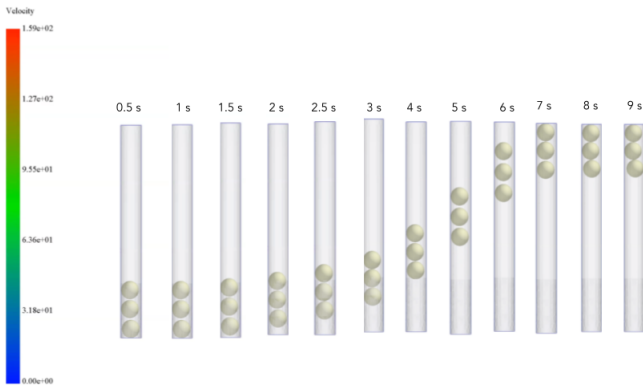


Figure 11: Frames of a coarse DEM simulation of a 1D setup.

Table 3: Data points of interest from experiments using a 13 cm bed height.

Inlet velocity (m/s)	Inlet pressure (psi)	Outlet pressure (psi)	Max height (cm)
0.300	0.234	0.000	13.5

4. Discussion

4.1. Experimental Results - Instabilities

The primary instabilities found in the simple cylinder set-up include: slug flow (oscillating bed variation), packed outer column formation due to electrostatic and friction forces between particles, packed particles in constrained top configuration, bed spout height settling. Slug flow is a form of burst instability where in the fluidized bed spurts sections of particles in an oscillatory manor. Each figure in Appendix B shows one or more of these instabilities.

4.1.1. Constrained Fluidized Beds

In the described vertical and horizontal theoretical configurations, the Boron pellets would be constrained to prevent pneumatic transport (mass transport) out of the fluidized bed which may occur due to the high inlet velocities required for heat exchange. Pneumatic transport will occur when the gas velocity is greater than the terminal velocity of the particle. The terminal velocity is found by first calculating the dimensionless particle diameter developed by Haiden and Levenspiel [6, cited by 7], equation C.9, which is then used to find the dimensionless terminal velocity approximated by Turton and Clark [10, cited by 7], equation C.7. This equation can be simplified to C.8 for perfectly spherical particles and is therefore useful for simulation estimations. The dimensionless terminal velocity then relates to the terminal velocity through Haiden and Levenspiel's approximation, equation C.10 [6, cited by 7]. All subscripts used in these equations are defined in Table C.6. The theoretical hollow annulus is not a geometry that we extensively tested and may result in unexpected particle packing. This problem may be exacerbated in a setup with a large amounts of unfilled space when settled and therefore this space should likely be minimized by having most of the available space filled. In Figure B.28 the

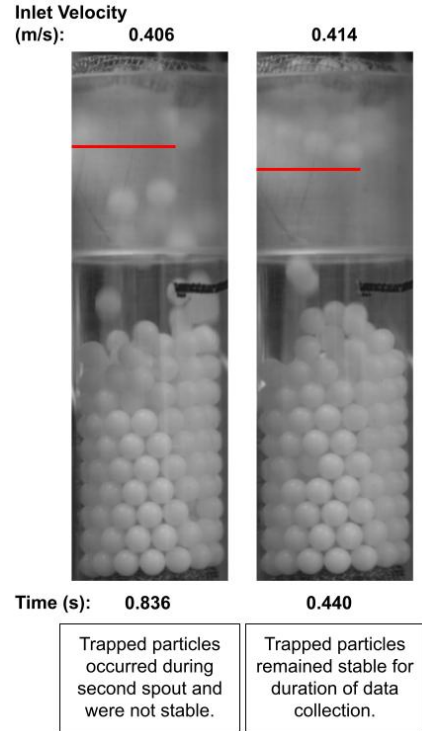


Figure 12: This figure shows the effect increasing the inlet velocity had on the number of trapped particles and their stability over time. The experiment was conducted with a starting bed height of 6 cm and diffused inlet velocity of 0.406 and 0.414 m/s.

inlet velocity was 0.406 m/s which was enough to, upon initial flow startup, result in sudden and semi-stable particle packing under the top mesh. It only occurred after the bed spouted high enough that enough particles came into the top section and became clogged with one another. If flow startup had occurred by going from 0.0 m/s and then slowly increasing to 0.406 m/s the bed's slugging behavior may have been different and would not have resulted in the sudden packed particles. However, after the inlet velocity was increased to 0.414 m/s, as shown in Figure 12, the particles became trapped more than once. This indicates even a subtle increase in inlet flow can affect the slugging behavior such that the frequency, magnitude, and stability of trapped particles may increase. More experimentation should be done into this phenomenon. In the untested annular geometry, locations of trapped particles may occur at a higher or lower frequency; however, consistent neutron shielding and heat exchange that requires homogeneous fluidization is imperative which makes locations of trapped particles dangerous. As will be discussed later, the final design is likely to need some agitator for which its effect on particle trapping needs to be researched further.

4.1.2. Particle Size

Introducing an agitator could also prevent the formation of an outer cylindrical particle shell and reduce slug flow fluidization. Reducing slugging is valuable because slugging leads to large gaps neutron shielding capabilities. Slugging



Figure 13: This figure shows the initial height progression of where bed separation occurs. Additionally the conical formation of the outer layer is shown. This occurred with the bottom mesh set up with a starting bed height of 18.5 cm and an inlet velocity of 0.397 m/s.

entails groups of particles rise and fall together creating an oscillating pattern throughout. This would result in pockets of undistributed heat. Where as, in homogeneous and turbulent fluidized bed the frequency of particle to particle and particle to wall interaction would facilitate heat exchange and there would be appropriate coverage for shielding purposes.

During experimentation an outer cylindrical shell of particles regularly formed during fluidization. This is likely due to a combination of electrostatic and friction forces between the particles themselves and the particles with the wall. This outer shell increased the height of where bed separation occurred during slugging and reduced how many particles were actively fluidized. If such a formation happened in the horizontal or vertical annular set-up it would create pockets of heat that would change how heat exchange occurred throughout the system. Consistent heat exchange is desired and therefore pockets and patterns such as this are not ideal. Additionally shell did impact how the dynamics of the rest of the bed and would likely also due so in the theoretical set-ups, as such, an agitator would be useful in preventing this.

At low inlet velocities after initial spurring behavior the fluidized bed was seen to settle as seen in Figure B.30. This phenomenon not expected to occur in the theoretical set-up due to high inlet velocities and is therefore not a thing of great consideration.

4.2. Ansys Simulations

The particle wakes displayed the greatest instabilities given rising inlet velocity. At high inlet velocities particle wakes pointed in varying directions; however, the general shape of the flow stayed consistent given differing geometries, inlet velocities, and flow models. The velocity profile, in Figure 9 displays how the inlet flow moves around the particles. The greatest velocity is seen in the the slipstreams between particles where the flow had easy access to the outlet. The 1D velocity data, for a line rake along the central axis of the geometry, showed its peak in between particles. In between particles there is a low pressure region that occurs as the available area widens and the velocity increases as a result.

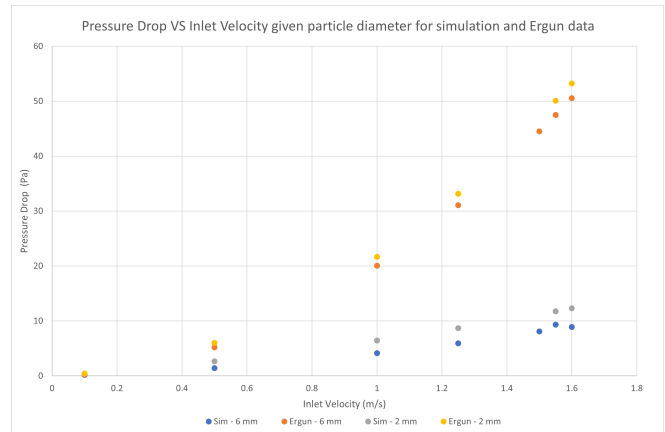


Figure 14: Pressure drop versus inlet velocity given varying particle diameters for simulation and Ergun pressure drop calculation methods. Simulation pressure drop measurements were approximately taken from 0.003138 m and 0.135147 m along the 6 mm geometry and from 0.000903 m and 0.0451 m along the 2mm geometries. This locations were chosen as the first and last middle sections between particles.

When running simulations determining the appropriate flow model is important in getting accurate data and understanding the state of the flow. All flow models had a no-slip boundary condition which can be seen in the gradient of the flow near particles where the flow velocity is reduced. From 0.1 to 300 m/s the laminar and low turbulence flow model fit the data while the high turbulence flow model fit the flow more accurately at 350 m/s. The pressure drop across the geometries as linear. Furthermore, in Figure A.16, the relationship between pressure drop and inlet velocity was linear. In literature, the standard expectation is that eventually the pressure drop plateaus after a minor decrease in the rising pressure drop [9, cited by 7]. The simulated data does not show a distinctive indication of this occurrence. For the simulated 6 mm geometry, in Figure 14, the data at 1.55 m/s is 0.439 pa above the pressure drop at 1.60 m/s. This could be the first sign of a subsequent plateau. Unfortunately, there is not enough data to corroborate this and it could be the result of a simulation meshing difference such that the 1.55 m/s run had a more refined mesh. More data needs to be collected around these inlet velocities with a more refined mesh. Additionally, it may not mathematically follow that the simulation data would show this plateau because the simulation set-up lacks a gravitational relationship between the parti-

cles and the fluid because the Ansys simulations were all conducted assuming a fixed particle geometry, therefore, the fluid is the only component that experienced the force gravity. This may explain part of the difference between the simulation data and the estimated Ergun pressure drop, C.3 [4], as the particle to fluid interactions were not comparable. Voidage fraction needed in Ergun's equation was calculated using equation C.11. A better model needs to be used where in the flow needs to overcome both gravity and the weight of the particles. In a complex horizontal annular setup the relationship between pressure drop and particle weight would be further complicated by disproportional gravitational effects of gravity. For instance along the top of the central cylinder particles would be present but their weight is accounted for in the normal force of the central cylinder. This would change what forces are needed to fluidize that portion of the fluidized bed. The effect of gravity on a fluidized bed cannot be understated and is shown by the disparity in estimated total bed pressure drop seen in Figure 14. The calculated Ergun pressure drops were consistently larger than the simulated pressure drop and increased at a greater rate than the simulated data. More simulations need to be conducted in order to understand the effect of particle to particles distance, non-idealized geometries (non-FCC configurations), inlet velocities that result in transitional flows. The fixed particle geometry means Ansys simulations are useful in understanding the flow but more research and time needs to be devoted to DEM-CFD in order to understand the particle movement as well.

4.3. DEM

4.3.1. 1D

The DEM simulations proved unreliable in terms of showing what layer fluidization starts. Software limitations prevent the balls to start at rest due to gravity prior to adding in the flow effects. Nonetheless, the simultaneous fluidization in this setup contrasts with the layer-by-layer fluidization found in the experimental observations. The space between the balls may allow the effective weight to be smaller than that of stacked balls, creating a net movement upward for each ball. The difference between a spaced starting configuration vs. a static starting configuration should be further investigated.

4.3.2. Single-cylinder setup

Based on the two results, the results are inconclusive as the simulations repeatedly showed lack of fluidization even in inlet velocities beyond the experimentally observed fluidization velocities.

4.4. Combining Simulations, Experimentation, and Theory

The goal during the research process was to combine the conceptual understanding found from the simulations, experiments, and available research. Research in fluidized beds is highly scenario specific, therefore breaking down the research into components and heavily understanding each parameter is how the full physical and fluid dynamics of the system can be comprehended and taken advantage of. For instance, the ratio

of particle to fluid density shows up in the Reynolds's number, equation C.6, and Archimedes' number, equation C.4 of the flow. These can be related to one another using Wen and Yu's relationship, equation C.5 [11, cited by 3] and used to predict the minimum fluidization velocity [3]. This method did not fit our experimental results; however, they do serve as a basis for initial minimum velocity estimations. This is useful for experimentation and research into the basic dynamics of the flow however is less applicable for fluidized beds with high inlet velocities where the dynamics would be different. This may be due to the the large particle size used in this experimentation which has differing fluidizing dynamics than smaller particles and particles in groups A-C are more researched than group D particles. As a result, group D particles may not conform to the standard mathematical models present in current literature. Research into these mathematical models will influence scale-up procedures from experimental results to the full scale B^{10} pellet annular fluidized bed.

5. Summary and conclusions

5.1. Final design suggestions

X-ray shielding material required to capture 99.9% according to attenuation trends is 30 cm of shielding which translates to about 29 kg of boron, which for now can be assumed to be sufficient for neutron shielding. Pellet compositions would have smaller mass fractions of the heavier material and larger fractions of a lighter filler material to allow for simple fluidization operations.

Given that a desired fluidized bed is homogeneous, the recommended class of particles used are class B due to the wide range of fluidization phases possible with this class. However, fluidization in the vertical setup will likely not be limited by the ball diameter as The minimum requirements of fluidization will be overcome by heat transfer requirements that need high inlet velocities. At these high inlet velocities the terminal velocities of the particles will be overcome which means the finalized setup will require a blocked outlet that does not allow particle transfer. This is necessary in the horizontal annular setup as well. The horizontal configuration will lead to disproportionate effects of gravity in different areas of the geometry. This may result in unexpected fluidization patterns that need to be researched further. In order to enhance inlet flow performance, the inlet flow needs to have a large inlet area to encourage a distributed starting flow. The primary instabilities seen during experimentation could be mitigated through the use of an agitator. The form of such a device needs to be able to withstand the high temperatures and neutron effects of the environment, additionally, it should not create pockets of unshielded areas.

5.2. Future work

There are many areas that, although touched upon or researched thus far, need to be further expanded upon and understood in greater depth. Possible future areas of research include: complex simulation geometries (horizontal annulus), particle and flow interaction in complex setups, velocity flow

field for particle and bubble movement, simulations for heat transfer between particles and the working fluid, as well as, particle particle heat transfer, and simulations involving gravity and no gravity.

Further experiments should be conducted using a laser to measure voidage and slugging frequency, using a heated working fluid to study heat transfer, using different porous diffusers to understand gas distribution, and exploring methods for reducing electrostatic effects on particles. The following parameters and areas should be optimized: particle to fluid density ratios, diameter to bed diameter ratios, pressure profiles of plug flows as described in this research.

Experimental data is needed for the absorption/transmissivity with dependence on temperature of boron, or for the chosen microwave shielding material, in order to incorporate the 1.5 MW of power the synchrotron produces into the heat calculations. Transmission data for boron at 200 GHz is difficult to find, but it has been gathered that higher temperature correlates to higher absorption since boron has lower resistivity at higher temperatures. This will affect the desired working temperature of boron when considering its electrical conductivity.

Additionally, there are suggested DEM simulations that can reveal more about fluidization behavior: The 6 mm balls used classify under group D particles, as mentioned in section 4.1.2. To get a sense as for what particle size would exhibit better homogeneity, a group B particle size (smaller than that of group D) and a larger group D particle size (arbitrarily chosen to be 1.5x the 6 mm diameter) should be used using the same simulation geometry and inlet. Based on visual observations, the simulations can reveal what class best displays homogeneity due to its weaker oscillation behaviors and lower occurrences of high void fraction areas. Regarding cap height, more separate simulations should show that lowering cap height decreases oscillation effects.

In terms of heating, simplifying the bed as a porous material with given porosity and determining the inlet velocity flow rates required to maintain pellets below 1100 K (the critical temperature for boron’s electrical conductivity) is one approach in deciding on cooling operations.

Acknowledgements

Our deepest appreciation to Samuel Cohen for being a supportive and attentive mentor and advisor during our research. Sincerest thanks to Bruce Berlinger, Sangeeta Punjabi-Vinoth, Chris Galea, and Liam David for working with us and helping us whenever we sought theoretical and technical advice in the lab. Furthermore, thank you so much to the Program in Plasma Science and Technology (PPST) and the High Meadows Environmental Institute (HMEI) for backing our research.

Appendix A. Simulation Graphs and Data

Table A.4: Conducted Ansys Simulations with FCC geometry and laminar flow

Particle diameter (mm)	# of rows	Simulation meshing			Inlet velocity (m/s)
		Surface mesh	Periodic boundaries	Volume mesh	
6	2	-	y	-	0.1 0.25 0.5*
	10	0.0005	y	0.0002	0.1 0.5 1.0 1.25 1.5 1.55 1.60
2	2	-	y	-	0.1
	10	0.0001	y	0.000117	0.1 0.5 1.0 1.25 1.5 1.55 1.60 250* 300* 350*
1	10	0.0002	n	0.0000625	0.1 0.5 1.0

*These inlet velocities were run with laminar, low turbulence and high turbulence flow models, not only the laminar flow model.

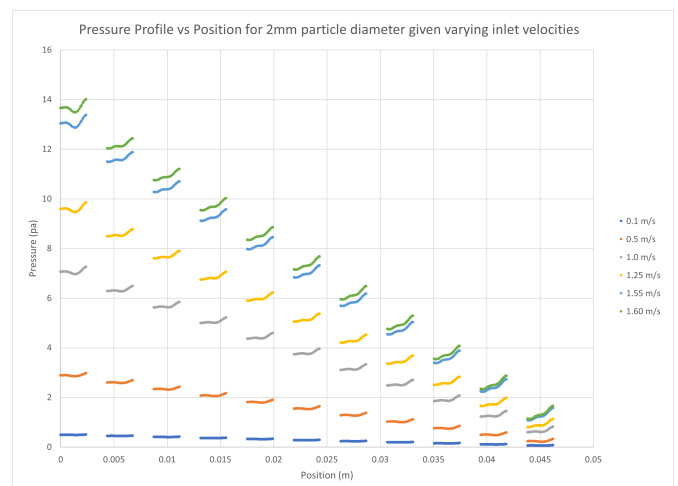


Figure A.15: 1D Pressure Profile through 10 row FCC configuration for 2 mm diameter particles.

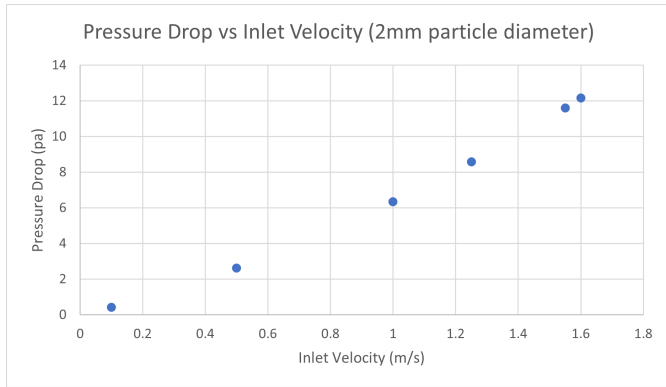


Figure A.16: Simulated pressure drop given varying inlet velocities for the 2 mm particle diameter configurations showing a linear pressure drop.

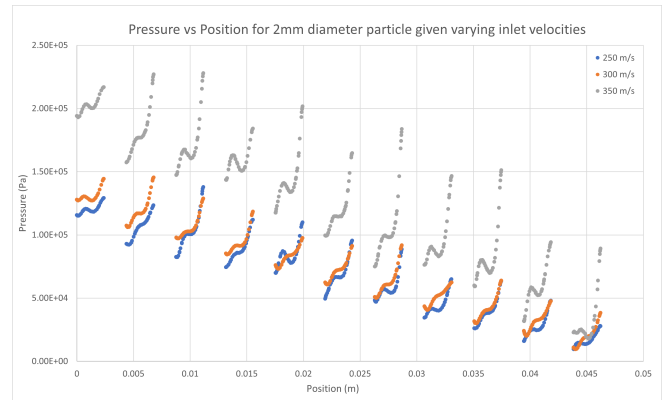


Figure A.19: 1D pressure profile for 2 mm diameter particle 10 row geometry with varying high inlet velocities.

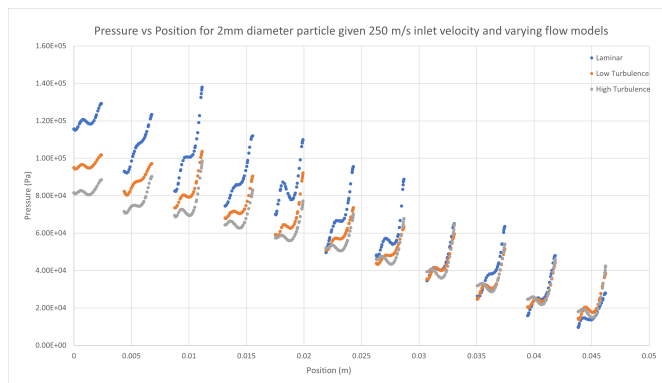


Figure A.17: 1D pressure profile for 2 mm diameter particle 10 row geometry with an inlet velocity of 250 m/s given varying flow models.

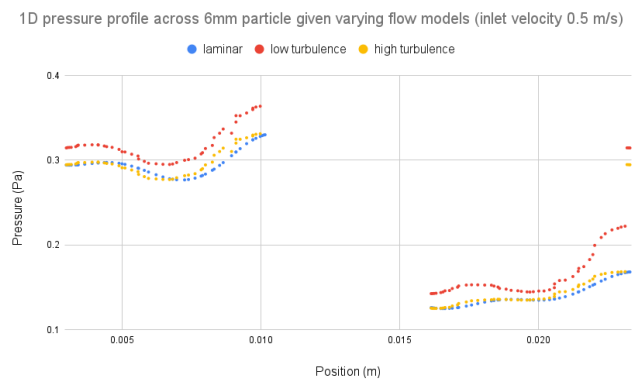


Figure A.20: 1D pressure profile for 6 mm diameter particle 2 row geometry with flow models at 0.5 m/s inlet velocity.

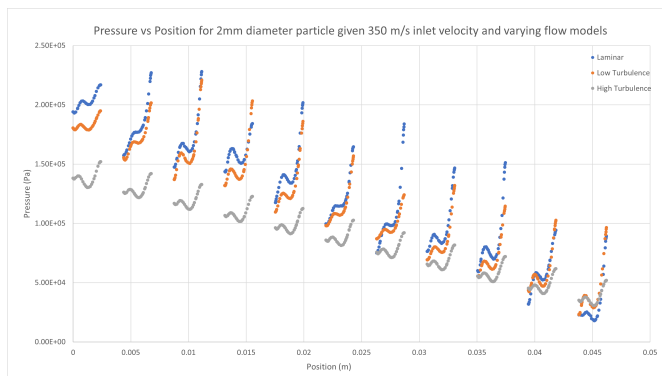


Figure A.18: 1D pressure profile for 2 mm diameter particle 10 row geometry with an inlet velocity of 350 m/s given varying flow models.

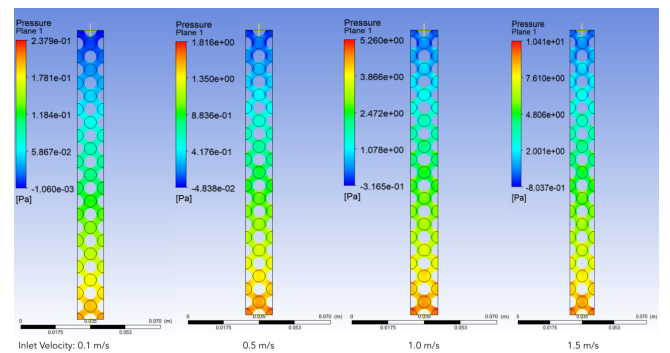


Figure A.21: 2D pressure profiles given varying inlet velocities for 6 mm particle diameter configurations showing flow pressure patterns. Increasing instability is seen with increasing velocities.

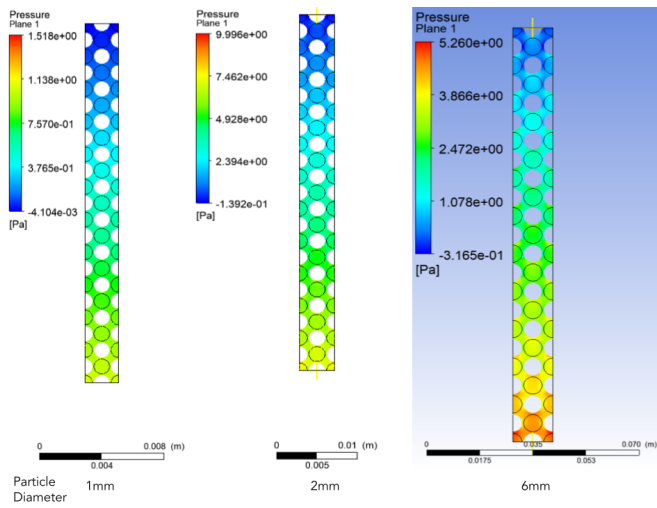


Figure A.22: 2D pressure profiles for varying particle diameter geometries with a consistent inlet velocity of 1 m/s.

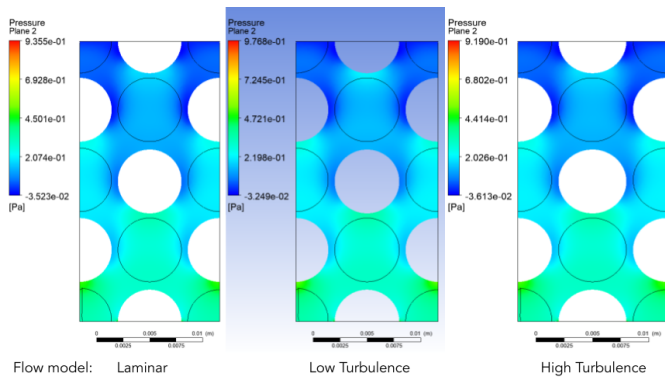


Figure A.23: 2D pressure profiles for 6 mm particle diameter geometries with an inlet velocity of 0.5 m/s given varying flow models.

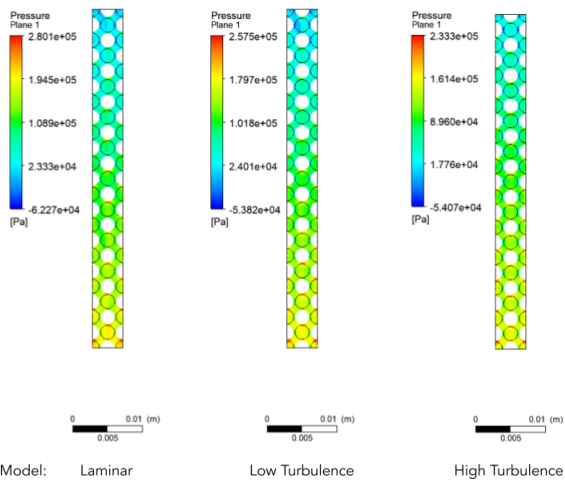


Figure A.24: 2D pressure profiles for 2 mm particle diameter geometries with an inlet velocity of 350 m/s given varying flow models.

Appendix B. Experiment Data and Graphs

Appendix B.1. Experiment Graphs

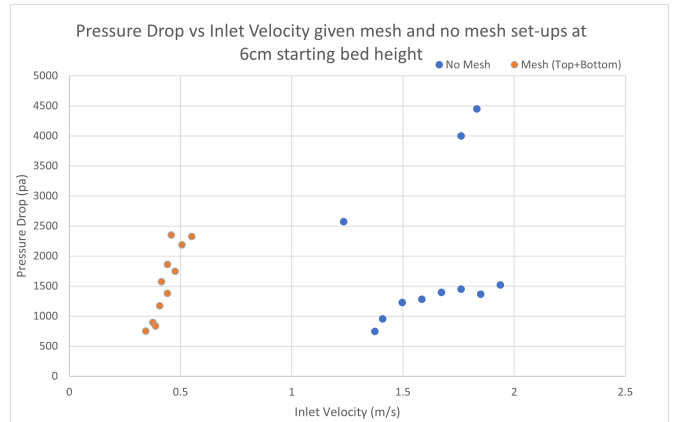


Figure B.25: Experimental pressure drop versus inlet velocity for 6 mm Delrin particles with the no mesh and full mesh (top and bottom) set-up, as seen in Figure 6.

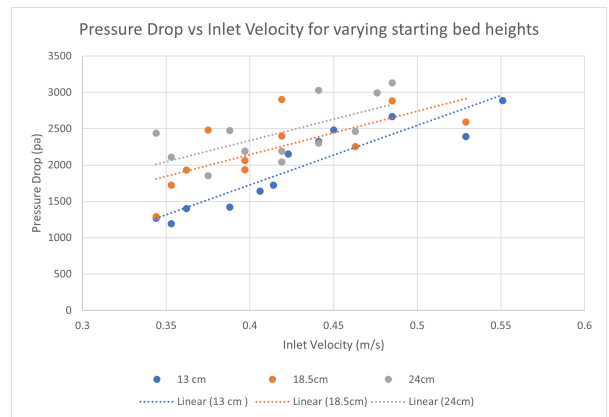


Figure B.26: Pressure drop versus inlet velocity for 6 mm Delrin particles with varying initial bed heights with mesh on the bottom as shown in Figure 6.

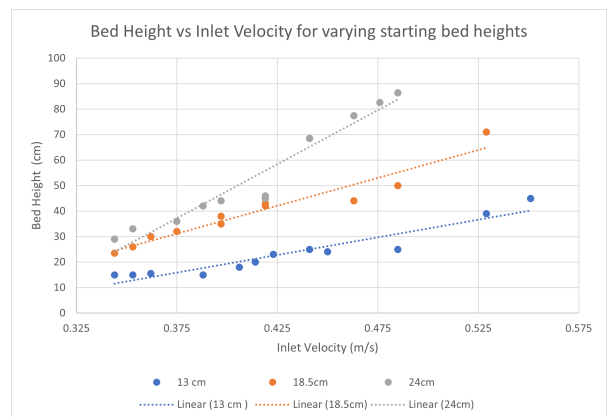


Figure B.27: Bed height versus inlet velocity with varying initial bed heights given 6 mm Delrin particles, air as the working fluid, and the bottom mesh configuration.

Appendix B.2. Experiment Fast Camera Images

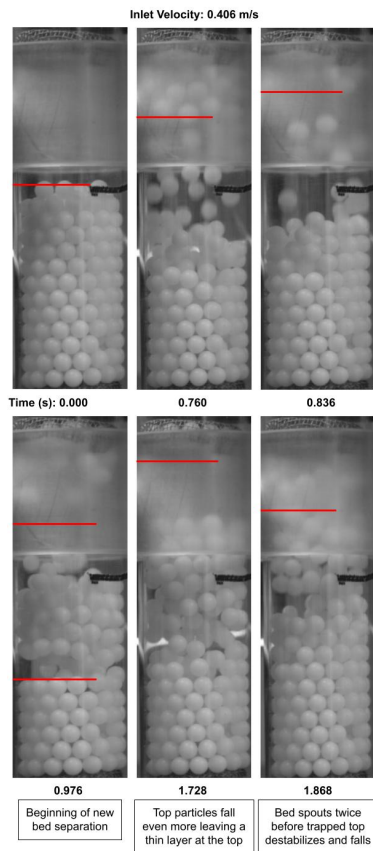


Figure B.28: This figure shows a possible effect of limiting particle movement by capping the highest bed height possible. The experiment was conducted with a starting bed height of 6 cm and an inlet velocity of 0.406 m/s.

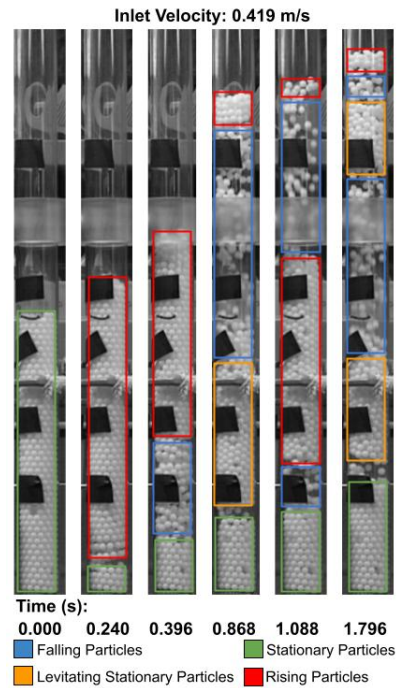


Figure B.29: This figure shows the particles separating into multiple different rising, levitating, and falling sections. This figure shows this for 24 cm starting bed height and a diffused inlet velocity of 0.419 m/s.

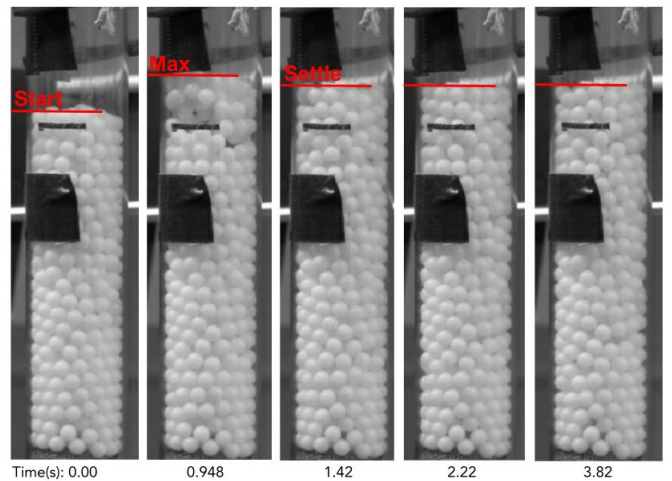


Figure B.30: This figure shows the start up max height into a settled bed height for the bottom mesh set up with a starting bed height of 13 cm and an inlet velocity of 0.310 m/s.

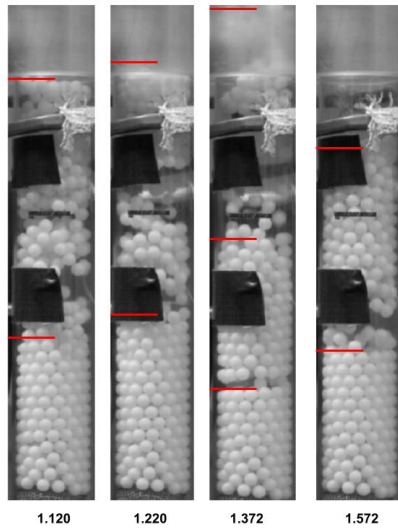
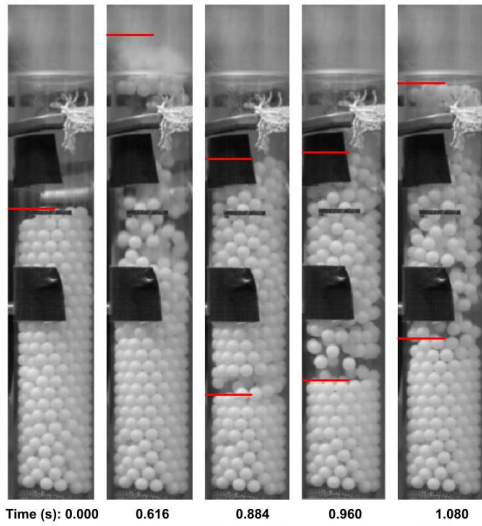


Figure B.31: This figure shows the start up max height into an spouting and oscillating bed height pattern. This occurred with for the bottom mesh set up with a starting bed height of 13 cm and an inlet velocity of 0.388 m/s .

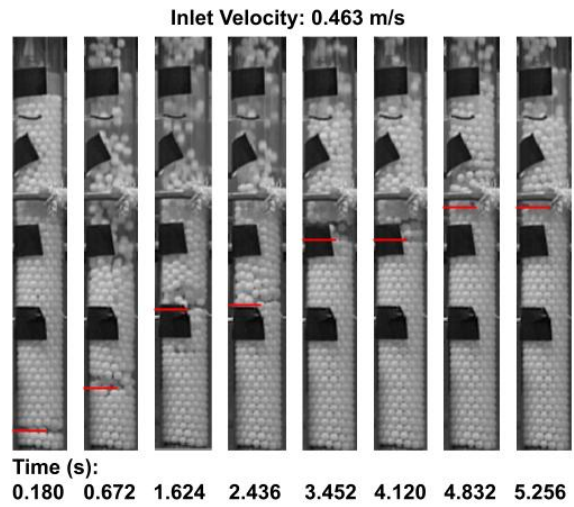


Figure B.32: This figure shows the initial height progression of where bed separation occurs which is likely a result of the conical stability of the bottom bed formation. This occurred with the bottom mesh set up with a starting bed height of 24 cm and an inlet velocity of 0.463 m/s .

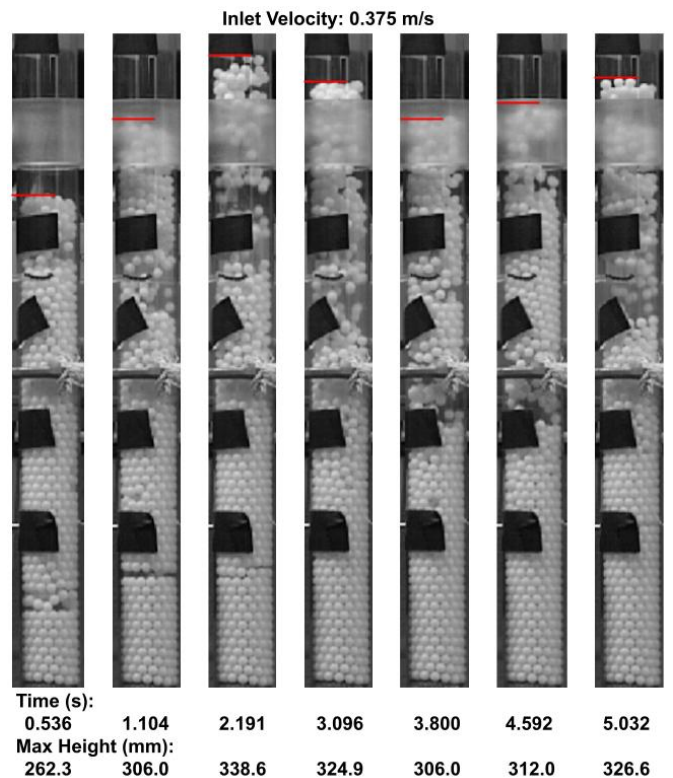


Figure B.33: This figure shows the varying max burst heights that occur over the course of the slugging flow. This occurred with the bottom mesh set up and a starting bed height of 24 cm and an inlet velocity of 0.375 m/s .

Appendix C. Equations and relevant parameters and constants

Appendix C.1. Experimental Safety Calculations

Bursting Pressure [8]

$$P = \frac{2 * S * t}{OD * SF} \quad (C.1)$$

Collapsing Pressure [12]

$$P = 0.807 * \left(\frac{E * t^2}{Lr} \right) * \sqrt[4]{\left(\frac{1}{1 - \nu^2} \right)^3 * \frac{t^2}{r^2}} \quad (C.2)$$

Appendix C.2. Theoretical Calculations

Ergun Equation [4, cited by 7]

$$\frac{\Delta P}{L} = \frac{150(1 - \epsilon)^2}{\epsilon^3} * \frac{\mu_g u}{(\phi_s d_p)^2} + \frac{1.75(1 - \epsilon)}{\epsilon^3} * \frac{\rho_g u^2}{\phi_s d_p} \quad (C.3)$$

Appendix C.2.1. Predicting Minimum Fluidization Velocity

Archimedes' Number [3]

$$Ar = \frac{\rho_g d_p^3 (\rho_p - \rho_g)}{\mu^2} \quad (C.4)$$

Relationship between Archimedes' Number and Reynold's number [11, cited by 3]

$$Ar = 1650 Re_{p,mf} + 24.5 Re_{p,mf}^2 \quad (C.5)$$

Reynold's Number at minimum fluidization [3]

$$Re_{p,mf} = \frac{\rho_g u_{mf} d_p}{\mu} \quad (C.6)$$

Appendix C.2.2. Approximating Terminal Velocity

Dimensionless terminal velocity approximated by Turton and Clark for $0.5 < \phi_s < 1$ [10, cited by 7]

$$u_t^* = \left(\frac{18}{(d_p)^2} + \frac{2.335 - 1.744\phi_s}{(d_p)^{0.5}} \right)^{-1} \quad (C.7)$$

Simplified dimensionless terminal velocity for $\phi_s = 1$ approximated by Turton and Clark [10, cited by 7]

$$u_t^* = \left(\frac{18}{(d_p^*)^2} + \frac{0.591}{(d_p^*)^{0.5}} \right)^{-1} \quad (C.8)$$

Dimensionless Particle Diameter developed by Haider and Levenspiel [6, cited by 7]

$$d_p^* = d_p \left(\frac{\rho_g (\rho_p - \rho_g) g}{\mu^2} \right)^{1/3} \quad (C.9)$$

Dimensionless to dimensional terminal velocity from Haider and Levenspiel [6, cited by 7]

$$u_t^* = u_t \left(\frac{\rho_g^2}{\mu(\rho_p - \rho_g)g} \right)^{1/3} \quad (C.10)$$

Appendix C.3. Working Calculations

Voidage Fraction

$$\epsilon = \frac{(\text{volume}_{total\ avail}) - (\text{particle volume}_{total})}{\text{volume}_{total\ avail}} \quad (C.11)$$

Appendix C.4. Simulation CAD Calculations

Smallest Distance Between Particles

$$d_{sc} = \frac{1}{10} * d_p \quad (C.12)$$

Unit Cell Height - Face Centered Cubic Configuration

$$UCH = 2 \sqrt{\frac{(d_p + d_{sc} d_p)^2}{2} - \left(\frac{d_p}{2} \right)^2} + d_p \quad (C.13)$$

Simulation Bed height

$$SBH = \# \text{ of rows} * \text{Unit Cell Height} \quad (C.14)$$

Table C.5: Nomenclature

Symbol	Unit	Meaning
Δp	pa	Pressure Drop
P	pa or psi	pressure
L	m	Length Constant
ϵ	-	Voidage Fraction
u	m/s	Superficial Velocity
μ	$\frac{kg}{m*s}$	Viscosity
d_p	m	Particle Diameter
r	in	radius
ρ	$\frac{kg}{m^3}$	Density
ϕ_s	-	Sphericity
ν	-	Poisson's Ratio
Re	-	Reynold's Number
Ar	-	Archimedes' Number
S	psi	Tensile Strength
E	psi	Elastic Modulus
OD	in	Outer Diameter
t	in	Cylinder Thickness
SF	-	Safety Factor
d_{sc}	in	smallest distance scale

Table C.6: Subscripts

Symbol	Meaning
p	Particle
g	Gas or working fluid
mf	Minimum fluidization
sc	smallest scale

Table C.7: Relevant Material and Chemical Constants

Name	Unit	Value	Conditions
Boron density	$\frac{kg}{m^3}$	2340.0	STP
Helium density [2]	$\frac{kg}{m^3}$	0.004012	1200K & 0.01 Mpa
Delrin density	$\frac{kg}{m^3}$	1420.0	-
Air density	$\frac{kg}{m^3}$	1.293	STP
Helium viscosity [2]	$\frac{kg}{m*s}$	$5.25 * 10^{-5}$	1200K & 0.01 Mpa
Air viscosity	$\frac{kg}{m*s}$	$1.81 * 10^{-5}$	STP
Packing efficiency	-	58%	-
Gravity	m/s^2	9.81	-
Polycarbonate tensile strength [1]	psi	9500	-
Polycarbonate elastic modulus [1]	psi	$3.75 * 10^5$	-
Polycarbonate Poisson's ratio [1]	-	0.36	-

References

- [1] Joan Agranoff. *Modern plastic encyclopedia*. McGraw-Hill, 1976.
- [2] Vincent D Arp, Robertnbsp; D McCarty, and Danielnbsp; G Friend. Thermophysical properties of helium-4 from 0.8 to 1500 k with pressures to 2000 mpa. *NIST - United States Department of Commerce*, 1998.
- [3] R. Cocco, S. Karri, and T. Knowlton. Introduction to fluidization. *AIChE Journal*, page 22, Nov 2014.
- [4] S. Ergun. Fluid flow through packed columns. *Chemical Engineering Progress*, 48(2):89, 1952.
- [5] Kevin P. Griffin and et al. Matthew T. Walsh. Effects of neutron radiation and shielding recommendations for the pfr4. *PPST Undergraduate Internship Program Participants*, page 610–612, 2014.
- [6] A. Haider and O. Levenspiel. Drag coefficient and terminal velocity of spherical and nonspherical particles. *Powder Technology*, 58(1):63, 1989.
- [7] Daizo Kunii and Octave Levenspiel. *Fluidization and Mapping of Regimes*. Butterworth-Heinemann, 2nd edition, 1991.
- [8] American Piping Products. Barlow equation, May 2021.
- [9] T. Shirai. Fluidized beds. *Kagaku-Gijutsu-Sha*, 1958.
- [10] R. Turton and N.N. Clark. An explicit relationship to predict spherical particle terminal velocity. *Powder Technology*, 53(2):27, 1987.
- [11] C. Y. Wen and Y. H. Yu. A generalized method for predicting the minimum fluidization velocity. *AIChE Journal*, 12(3):610–612, 1966.
- [12] Warren C. Young, Richard G. Budynas, and Raymond J. Roark. *Roark's formulas for stress and strain*. McGraw-Hill, 7 edition, 2002.